

Thermoelastic Response Analysis of a Shape Memory Alloy Wire Embedded Active Hybrid Bimorph Composite



Rupal Srivastava  and Bishakh Bhattacharya 

Abstract The class of metallic alloys that show the ability to memorize its shape at a specific temperature and recover large deformations on thermal activation are called Shape Memory Alloys (SMA). SMA wire-based Hybrid Composites (SMAHC) is a continuously emerging research area given their versatile applications within the domain of active shape morphing, structural control, deployable space mechanisms, and other adaptive characteristics. We study the simulated behavior of an Active Bimorph Structure (ABS) composed of embedded SMA wires within a fiber-reinforced composite, modeled and analyzed in ABAQUS. The wires are embedded in two layers of the composite at 0° and 90° to obtain a bidirectional bending from the system. The SMAHC plate is fixed at one end and free at another, by introducing heat into the system we observe the deflection obtained. The SMA wires are assumed as fibers and analyzed based on their volume fraction. Further, different orientation angles of wires and boundary conditions are studied to compare the variation in tip displacement of the SMAHC. Various permutations of fiber-matrix combinations are also explored, based on the variation of fiber stiffness—a function of SMA fiber volume fraction, SMA fiber ply thickness, etc. It was observed that with increasing the ply layout in two-layer SMA fiber-reinforcement, a significant bidirectional bending was obtained. It was also found that twisting can be extracted from the plate by varying the SMA fiber orientation angle. The aim of this paper is to model a Deployable Active Bimorph Box Structure (ABBS) such that when the SMAHC is subjected to a thermal field, it first transforms into a cylinder and then into a curved cylindrical element.

Keywords Shape memory alloy · Smart laminated composites · Active bimorph structure · Deployable structure · Thermoelastic response analysis

R. Srivastava (✉) · B. Bhattacharya
Department of Mechanical Engineering, Indian Institute of Technology Kanpur, Kanpur, India
e-mail: rupalsri@iitk.ac.in

B. Bhattacharya
e-mail: bishakh@iitk.ac.in

© Springer Nature Singapore Pte Ltd. 2021
E. J. Sapountzakis et al. (eds.), *Proceedings of the 14th International Conference on Vibration Problems*, Lecture Notes in Mechanical Engineering, https://doi.org/10.1007/978-981-15-8049-9_9

1 Introduction

The increase of space exploration triggered the requirement of lower launch costs, and hence, the need for deployable structures came into existence. Deployable structures are structures having a small stowed volume, which upon inflation and rigidization expand manifold and gain the required size and shape. Some of the early and notable examples of deployable structures are the Goodyear's inflatable search radar antenna technology, NASA ECHO (I and II) communication balloon satellite experiments carried out in the 1960s, followed by the Inflatable Antenna Experiment in the 1990s [14]. To carry out these experiments, conventional rigidization methods like chemically loaded gas-based inflation and curing through membrane impregnated with resin [7] and ultra-violet rays/photo-initiated cationic-based curing [1] were employed. However, these methods had their disadvantages like outgassing in gas-based inflation and uncontrollable rigidization in case of UV-based process due to shadowing. Hence, a constant lookout for novel deployment and rigidization method is undergoing. Some of these innovative methods that are being explored at laboratory levels are Electrostatic Inflation [27] and utilization of embedded Shape Memory Alloy (SMA) wires for rigidization.

Buehler and Wiley from the Naval Ordnance Laboratory (NOL), in 1965, invented a series of unique Nickel–Titanium alloys that possessed mechanical memory and called it NiTiNOL that falls under the broad category of SMAs [6]. This unique property results from the reversible diffusion-less solid-to-solid phase transformation from austenite to martensite. It was also determined that to control SMA efficiency we could change the percentage of Nickel and Titanium, which changed the transformation temperatures in the material. The specific energy density of SMAs was found to be the highest in comparison to known actuators, they give a large force-output/weight ratio, large stroke, and are also flexible, compact, and environment friendly.

Raychem Corporation carried out the first successful application of SMA in an F-14 aircraft's hydraulic system. The idea of embedding SMAs in a laminated polymer matrix composite (PMC) was first given by Rogers and Robertshaw [22] and has since been used in the field of structural health monitoring [21], active jet engine chevrons [13], and also for active aircraft wing shape morphing [25]. This integration of SMA with composite structures resulted in several applications such as vibration control [23], shape control [8], robot grippers [11], in-flight tracking of helicopter rotor-blades [10], etc. Some experiments have also been carried out to employ the use of SMA for deployment purposes [26]. Much work has been done to model the behavior of Shape Memory Alloys experimentally, mathematically, and numerically. Several quasi-static models, such as Tanaka model [28], Liang and Rogers' [18], Brinson's [5], and Boyd and Lagoudas' model [4] as well as steady-state models like Turner's Recovery Stress Model (RSM) and Effective Coefficient of Thermal Expansion (ECTE) model [29], and continuum-based model [24] are available in the literature. For simulation purposes using Finite Element Methods based tools like ABAQUS and ANSYS, a UMAT is used to define the SMA's nonlinear behavior

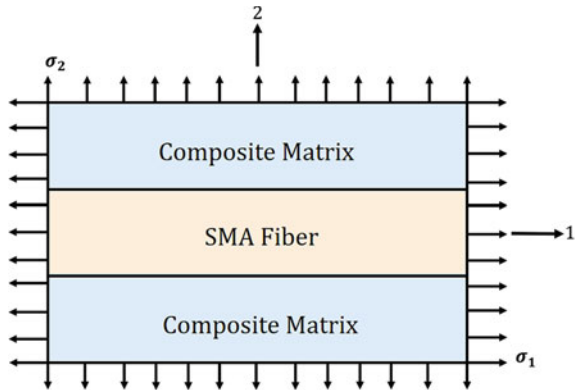
[17] in ABAQUS, whereas ANSYS has its built-in model for Superelasticity and Shape Memory Effect, using the Auricchio model [2]. Auricchio et al. has also given a simulation model for superelastic behavior of shape memory alloys [3], Ghomshei et al. [12] simulate an SMA embedded beam, Burton et. al. give a Finite Element Solution of a self-healing shape memory alloy composite, and more recently, Panda-Singh [20] conducted a thermal post-buckling analysis of a composite spherical shell embedded with SMA fibers.

The objective of this paper is to analyze the bending behavior of the composite with two layers of SMA wire/fiber-reinforcement and compare it with varying SMA fiber volume fractions and fiber orientations. This paper presents the results of the investigation in the following subjects:

1. Initially, a cantilever SMAHC is embedded with one layer of SMA fibers followed by two layers of SMA fiber- reinforcement.
2. In the next part, we consider both the sample cases with a fixed-fixed boundary condition.
3. We then carry out the static thermoelastic response analysis for the two boundary conditions and both of the sample cases.

Turner’s Effective Coefficient of Thermal Expansion Model The requirement of Turner’s ECTE model [29] comes when we require an alternative approach and employ a constitutive model that uses experimental measurements of the shape memory alloy. A representative volume element employed in this model is shown in Fig. 1. This element is considered in the plane of the plate, the principal material directions are 1 and 2, wherein the SMA wire is embedded along 1-direction.

Fig. 1 Volume element of the SMAHC lamina [29]



For a SMAHC lamina of Glass-Epoxy embedded with NiTiNOL wires, adding the thermal expansion behavior of NiTiNOL from Turner, Zhong, and Mei [30] to the 1D uniaxial thermoelastic constitutive relation by Jia and Rogers [15]:

$$\sigma_{1a} = E_a \epsilon_1 + \sigma_r \quad T \geq A_s \quad (1a)$$

$$\sigma_{1a} = E_a (\epsilon_1 - \alpha_{1a} \Delta T) \quad T < A_s \quad (1b)$$

Here, E_a is the Young's Modulus of the SMA, ϵ_1 is the strain in 1-direction (longitudinal), α_{1a} is the coefficient of thermal expansion for SMA when temperature T is less than the Austenite start temperature A_s , and σ_r is the recovery stress of the SMA when $T \geq A_s$. The uniaxial thermoelastic constitutive relation for SMA written in terms of Effective Coefficient of Thermal Expansion (ECTE) is

$$\sigma_{1a} = E_a \left[\epsilon_1 - \int_{T_0}^T \alpha_{1a}(\tau) d\tau \right] \quad (2)$$

From Eqs. (1a) and (2), we see that at temperature below Austenite start temperature,

$$\int_{T_0}^T \alpha_{1a}(\tau) d\tau = \alpha_{1a} \Delta T \quad (3)$$

and at temperatures above austenite start temperature,

$$\begin{aligned} \sigma_r &= -E_a \int_{T_0}^T \alpha_{1a}(\tau) d\tau \\ \text{or, } \int_{T_0}^T \alpha_{1a}(\tau) d\tau &= -\frac{\sigma_r}{E_a} \end{aligned} \quad (4)$$

Using this, we can capture the nonlinear thermoelastic behavior of the SMA. The constitutive equation for the transverse direction is

$$\sigma_{2a} = E_a \left[\epsilon_2 - \int_{T_0}^T \alpha_{2a}(\tau) d\tau \right] \quad (5)$$

In case of reinforced SMA wires unidirectionally along 1-direction α_{2a} is not related to recovery stress but is linear due to change in martensite fraction. Thus, the thermoelastic constitutive relations for an orthotropic lamina under plane stress becomes

$$\begin{Bmatrix} \sigma_1 \\ \sigma_2 \\ \tau_{12} \end{Bmatrix} = \begin{bmatrix} Q_{11} & Q_{12} & 0 \\ Q_{12} & Q_{22} & 0 \\ 0 & 0 & Q_{66} \end{bmatrix} \begin{Bmatrix} \epsilon_1 \\ \epsilon_2 \\ \gamma_{12} \end{Bmatrix} - \begin{bmatrix} Q_{11} & Q_{12} & 0 \\ Q_{12} & Q_{22} & 0 \\ 0 & 0 & Q_{66} \end{bmatrix} \int_{T_0}^T \begin{Bmatrix} \alpha_1 \\ \alpha_2 \\ 0 \end{Bmatrix} d\tau \quad (6)$$

where $[Q]$ is the reduced stiffness matrix. The relation between the reduced stiffness matrix and the engineering constant is discussed in the Appendix. The above constitutive relation is referred to as the effective coefficient of thermal expansion model (ECTEM). We employed ECTEM in our work due to the following reasons:

1. We do not require the superelastic effect for our constrained recovery analysis; this model suitably predicts the required Shape Memory Effect.
2. The model requires only four parameters- Austenite Start Temperature, Austenite Finish Temperature, Recovery Stress, and Young's Modulus, and we had resources available to calculate the same.

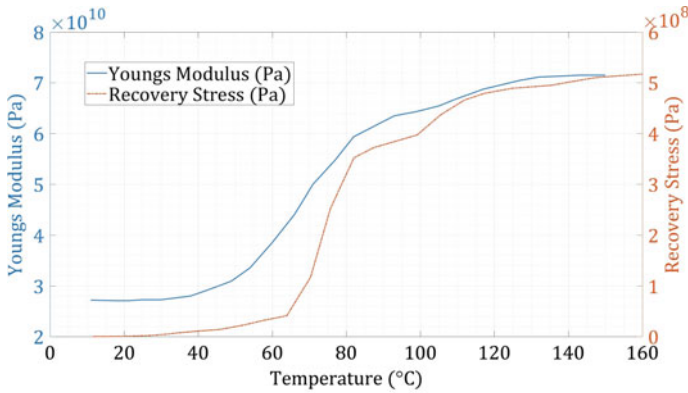
2 Design and Modeling

2.1 SMA Material Characterization

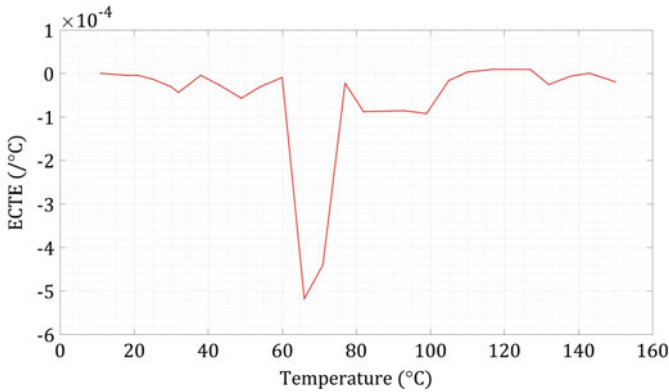
SMA wires, HT375, used for this study were procured from Dynalloy, Inc. Due to limited available data, material characterization according to the ECTE model requirement was carried out. As per the ECTE model, we find the dependence of the effective coefficient of thermal expansion (ECTE) against temperature, which is constant and takes a sudden jump as the austenite phase begins. Generally, for metals and alloys, the coefficient of thermal expansion is positive, however, SMA wires shrink with an increase in temperature as they convert from their martensite phase to the austenite phase. Hence, ideally for an SMA, we have the coefficient of thermal contraction (CTC). From Eq. (4) we see that we require to find the values of recovery stress (σ_r) and Young's modulus (E_a) to calculate the value of the effective coefficient of thermal expansion of the SMA (α).

Block Recovery Stress (σ_r) The test was conducted with help from National Aerospace Laboratories (NAL), Bangalore. A 4.5% of pre-strain was set in the wire before the test, the results of which are shown in Fig. 2a. The SMA wire was constrained in the crossheads of the tensile testing machine allowing no deformation. From there on, the voltage was increased using the SMA amplifier from 0 to 10 V. The SMA amplifier was turned off, and the crossheads of the tensile testing machine were calibrated for the load cell to indicate zero reading once 10 V was reached. The austenite finish temperature (A_f) increases with an increase in pre-strain and mechanical constraint [29].

SMA Young's Modulus (E_a) Tensile tests were conducted on a controllable environment Tinius Olsen machine. The loading rate was 0.6 mm/min, and the heating rate of the temperature chamber was 9°C/min. At room temperature, the specimen was loaded up to 30 N and unloaded to 0 N. In the second cycle the specimen was loaded to 60 N, and in the third cycle, it was loaded to 90 N before unloading. Finally, the specimen was loaded till failure which was found to be at 140 N. The same set of steps were repeated for varying temperatures, and the findings are summarized in Fig. 2a.



(a) Block Recovery Stress and SMA Young's Modulus vs Temperature [10]



(b) ECTE vs Temperature [10]

Fig. 2 Material characterization of SMA

The recovery stress σ_r and Young's Modulus E_a values were obtained at discrete temperature points, a spline curve capturing continuous values was constructed. Equation (4) was solved for α using the *cumtrapz* function in MATLAB and the results are shown in Fig. 2b. The obtained temperature-dependant ECTE data is input in the simulation done ahead.

2.2 Specimen Configuration

The numerical simulation in this paper has been done on two cases of SMA fiber-reinforced composite, SMA-based hybrid composite (SMAHC) with a single layer of SMA fiber embedded and the other with two layers of SMA fiber-reinforcement.

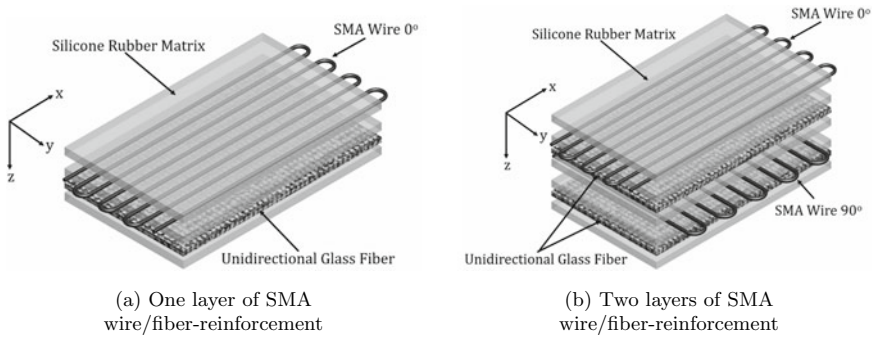


Fig. 3 Schematic of SMA wire embedded composite [26]

Table 1 Material properties of E-Glass fiber and silicone rubber

Properties	E-Glass fiber	Silicone rubber matrix
Young’s modulus (Pa)	72×10^9	0.001×10^9
Poisson’s ratio	0.21	0.47
Coefficient of thermal expansion ($10^{-6}/^{\circ}\text{C}$)	4.9	250
Density (Kg/m^3)	2600	2300

This is done to analyze the bidirectional bending of a SMAHC caused due to the embedding of SMA fibers in offset and actuated through resistive heating. Upon actuation, the layer which consists of SMA fibers tends to shrink whereas the one without, resists this deformation, causing the structure to deflect. When embedded in two layers, at 0° and 90° , we produce a bidirectional bending. The experimental study on active bimorph structures is done previously by the authors [26]. Figure 3a and b show the ply arrangement for the two cases.

The mechanical properties required to define the behavior of a composite are volume fraction of the fiber (V_f), volume fraction of the matrix (V_m)- $1 - V_f$, Young’s Modulus of the fiber (E_f) and the matrix (E_m), Poisson’s ratio of both fiber(ν_f) and matrix (ν_m), density ρ_f and ρ_m , and finally the coefficient of thermal expansion α_f and α_m . The materials selected for the analysis are E-Glass Fiber and Silicone rubber as the matrix. The material selection of the matrix was done considering the elastomeric property allowing large deformation. The properties used in the simulation are acquired from our material supplier and are tabulated in Table 1.

The equivalent orthotropic mechanical properties of the lamina are then calculated for both the layers, E-Glass-Silicone, and SMA fiber-Silicone using the Rule-of-Mixtures, and Halpin-Tsai equations [9], given in the Appendix. The temperature-dependent equivalent orthotropic mechanical properties of the SMA fiber-reinforced layer are collated in Table 3 and for the E-Glass Fiber-Silicone Rubber Matrix lamina in Table 2. The unit of measurement for these properties are in Pa for Young’s mod-

Table 2 Equivalent orthotropic material properties for E-Glass fiber-silicone rubber matrix lamina

E_1	$E_2 = E_3$	$G_{12} = G_{13}$	G_{23}	$\nu_{12} = \nu_{13}$	ν_{23}	α_1	$\alpha_2 = \alpha_3$	ρ
5.76×10^{10}	4.9997×10^6	1.7006×10^6	1.3060×10^6	0.262	0.9141	4.9009×10^{-6}	7.6959×10^{-5}	2540

ulus and Shear modulus, $^{\circ}\text{C}$ for the coefficient of thermal expansion, and Kg/m^3 for density (ρ). The fiber volume fraction of glass fiber is taken to be 0.8, and for the data shown in Table 3, volume fraction for SMA fiber is 0.9.

2.3 Finite Element Modeling

The static thermoelastic response analysis of both fixed-free and fixed-fixed conditions, for the two sample case, are carried out in ABAQUS. A plate of length 0.1, and 0.06 m width, and of 0.001 m thickness is modeled. Using the temperature-dependent attributes, the properties of the plate are defined for the two sample models, a two-ply composite $[0_{SMA}/0_f]$ and a four-ply composite $[0_{SMA}/0_f/90_{SMA}/0_f]$, here subscripts *SMA* and *f* denote SMA fiber ply and E-glass fiber ply respectively. The standard, linear quad S4R shell element type is incorporated to model the nonlinear material response and large deformations, and the meshing is completed through free technique, advancing front algorithm. Here, the dimensions of the samples are chosen based on in-lab experiments on similar models. After this, one side of the plate, along the longitudinal direction, is fixed, and a predefined temperature field is given to the cantilever in steps—where the steps are chosen based on sudden variation in effective coefficient of thermal expansion observed through experiment [ref. Figure 2b]. The temperature was increased in steps- 11–60, 60–66, 66–92, and 93–150 $^{\circ}\text{C}$, and the corresponding maximum deflection of the plate in z-direction was recorded. The thickness of the plate, fiber orientation angle, and volume fraction of SMA fiber-reinforcement is varied and compared. Next, we simulate the thermal response of the structure with fixed-fixed boundary condition.

3 Results and Discussion

The equivalent orthotropic properties for the E-Glass fiber-Silicone Rubber matrix ply and the SMA fiber-Silicone Rubber matrix ply were calculated using the Rule-of-mixture and Halpin–Tsai equations. It was found the ECTE along 1-direction (α_{11}), and Young's modulus along 2-direction (E_2) for SMA-Silicone ply remain constant with change in volume fraction of SMA (NiTiNOL) fibers, hence the variation of

Table 3 Equivalent temperature-dependent orthotropic mechanical properties for SMA Fiber (NiTiNOL)-Silicone rubber matrix lamina

T	E_1	E_2	$G_{12} = G_{13}$	G_{23}	$\nu_{12} = \nu_{13}$	ν_{23}	α_{11}	$\alpha_{22} = \alpha_{33}$	ρ
11	2.44E + 10	1.00E + 07	3.40E + 06	2.60E + 06	0.344	0.914	-1.76E-08	2.50E-05	5.66E + 03
18	2.44E + 10	1.00E + 07	3.40E + 06	2.60E + 06	0.344	0.914	-4.46E-06	2.10E-05	5.66E + 03
21	2.44E + 10	1.00E + 07	3.40E + 06	2.60E + 06	0.344	0.914	-4.51E-06	2.09E-05	5.66E + 03
25	2.45E + 10	1.00E + 07	3.40E + 06	2.60E + 06	0.344	0.914	-1.33E-05	1.31E-05	5.66E + 03
30	2.45E + 10	1.00E + 07	3.40E + 06	2.60E + 06	0.344	0.914	-3.07E-05	-2.65E-06	5.66E + 03
32	2.46E + 10	1.00E + 07	3.40E + 06	2.60E + 06	0.344	0.914	-4.38E-05	-1.44E-05	5.66E + 03
38	2.52E + 10	1.00E + 07	3.40E + 06	2.60E + 06	0.344	0.914	-4.75E-06	2.07E-05	5.66E + 03
43	2.63E + 10	1.00E + 07	3.40E + 06	2.60E + 06	0.344	0.914	-2.66E-05	1.09E-06	5.66E + 03
49	2.78E + 10	1.00E + 07	3.40E + 06	2.60E + 06	0.344	0.914	-5.71E-05	-2.64E-05	5.66E + 03
54	3.02E + 10	1.00E + 07	3.40E + 06	2.60E + 06	0.344	0.914	-3.11E-05	-2.97E-06	5.66E + 03
60	3.46E + 10	1.00E + 07	3.40E + 06	2.60E + 06	0.344	0.914	-9.42E-06	1.65E-05	5.66E + 03
66	3.96E + 10	1.00E + 07	3.40E + 06	2.60E + 06	0.344	0.914	-5.18E-04	-4.41E-04	5.66E + 03
71	4.49E + 10	1.00E + 07	3.40E + 06	2.60E + 06	0.344	0.914	-4.4E-04	-3.71E-04	5.66E + 03
77	4.92E + 10	1.00E + 07	3.40E + 06	2.60E + 06	0.344	0.914	-2.27E-05	4.56E-06	5.66E + 03
82	5.34E + 10	1.00E + 07	3.40E + 06	2.60E + 06	0.344	0.914	-8.81E-05	-5.43E-05	5.66E + 03
93	5.71E + 10	1.00E + 07	3.40E + 06	2.60E + 06	0.344	0.914	-8.60E-05	-5.24E-05	5.66E + 03
99	5.78E + 10	1.00E + 07	3.40E + 06	2.60E + 06	0.344	0.914	-9.26E-05	-5.83E-05	5.66E + 03
105	5.88E + 10	1.00E + 07	3.40E + 06	2.60E + 06	0.344	0.914	-1.66E-05	1.01E-05	5.66E + 03
110	6.02E + 10	1.00E + 07	3.40E + 06	2.60E + 06	0.344	0.914	2.90E-06	2.76E-05	5.66E + 03
117	6.18E + 10	1.00E + 07	3.40E + 06	2.60E + 06	0.344	0.914	9.32E-06	3.34E-05	5.66E + 03
127	6.34E + 10	1.00E + 07	3.40E + 06	2.60E + 06	0.344	0.914	9.18E-06	3.33E-05	5.66E + 03
132	6.40E + 10	1.00E + 07	3.40E + 06	2.60E + 06	0.344	0.914	-2.57E-05	1.88E-06	5.66E + 03
138	6.42E + 10	1.00E + 07	3.40E + 06	2.60E + 06	0.344	0.914	-6.20E-06	1.94E-05	5.66E + 03
143	6.43E + 10	1.00E + 07	3.40E + 06	2.60E + 06	0.344	0.914	2.40E-07	2.52E-05	5.66E + 03
150	6.43E + 10	1.00E + 07	3.40E + 06	2.60E + 06	0.344	0.914	-1.94E-05	7.53E-06	5.66E + 03

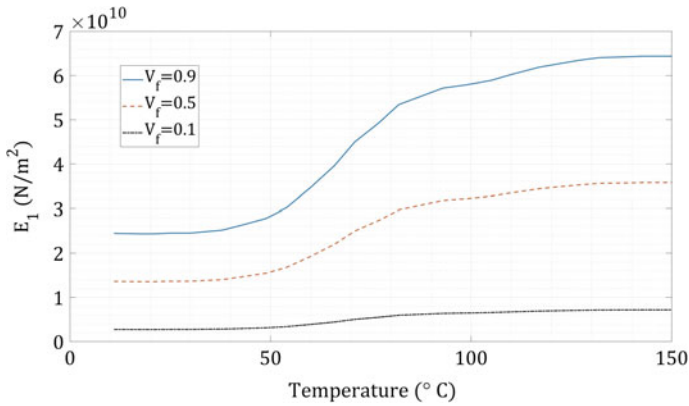


Fig. 4 Temperature versus longitudinal Young’s modulus (E_1)

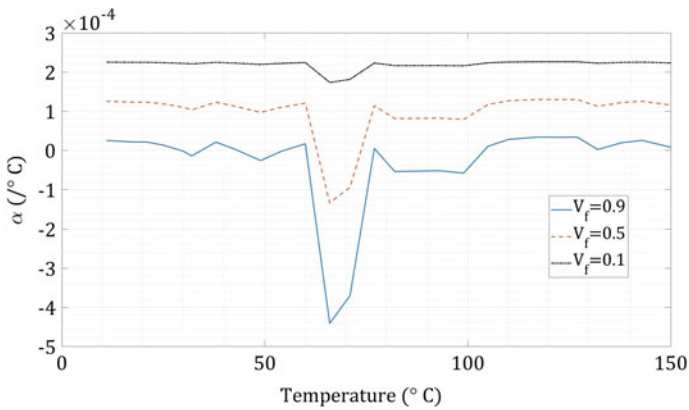
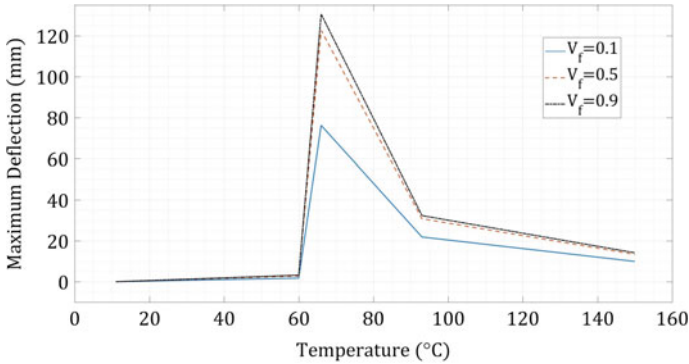


Fig. 5 Temperature versus ECTE along transverse direction (α_{22})

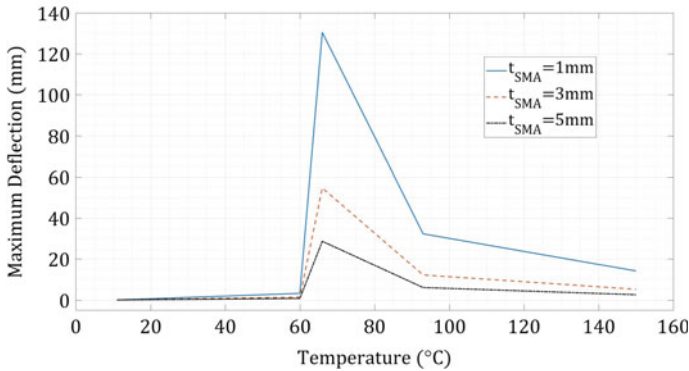
Young’s Modulus along 1-direction (E_1) and ECTE along 2-direction (α_{22}) play an important role in the out-of-plane deflection of the plate; this variation is plotted in Figs. 4 and 5.

It can be seen that with an increase in fiber volume fraction the equivalent Young’s Modulus of the SMA Fiber-Silicone Rubber Matrix along the longitudinal direction and the equivalent ECTE along the transverse direction increases.

Static Thermoelastic Analysis Meo et al. [19] showed that the introduction of SMA wires led to a reduction of interplay failure, thus allowing continuous stress transfer and increasing overall bending and shear elasticity upon impact. Here we do not include impact loads, however, upon application of a uniform temperature field which causes the SMA wires to shrink, the vertical bending of the plate increases with an increase in the fiber volume fraction of SMA. As suspected, this behavior can be seen in Fig. 6a. In the first case of our simulation, we considered three cases



(a) One layer of SMA fiber-reinforcement: Temperature vs. maximum deflection in the vertical direction when SMA fiber ply thickness (t_{SMA})=1mm



(b) One layer of SMA fiber-reinforcement: Temperature vs. Maximum deflection in the vertical direction when SMA fiber volume fraction (V_f)=0.9

Fig. 6 Case 1.1: One layer of SMA fiber-reinforcement: temperature versus maximum deflection in z-direction

of SMA fiber volume fraction 0.1, 0.5, and 0.9, whereas the fiber volume fraction of E-glass fiber in the second ply is kept constant at 0.8, and the thickness of the plies is 1 mm each. The initial deflection profile at room temperature is caused due to the geometric imperfection of the plate. As we can see in Fig. 3b, the plate acts as a linear thermoelastic body in the range of 11–60°C. At temperature above 60°C, we see a sudden change in the ECTE of SMA caused due to reverse-phase transformation, causing recovery stress, this recovery stress, in turn, generates in-plane tensile stresses. We see the maximum deflection along z-direction where the ECTE is highest (negative) and gradually decreases as the reverse-phase transformation is complete. This behavior is confirmed with the work done by Brian et al. for a fixed-fixed boundary condition. It was observed that when the SMA fibers were at

an orientation other than 0° , the plate underwent a slight twist, but in all the cases the major deflection was observed in $U3/z$ /out-of-plane/vertical direction. Thus, to avoid redundancy, the maximum vertical deflection of the plate is recorded and reported.

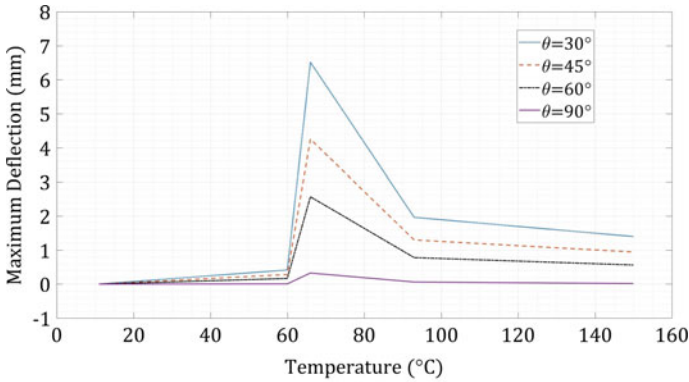
We next analyze the effect of the increase in ply thickness of SMA fiber lamina (t_{SMA}) on the vertical displacement by keeping the SMA fiber volume fraction constant. As we saw in the case of 1 mm thickness ply, the maximum deflection along z-direction was obtained when the SMA fiber volume fraction was 0.9; thus we consider these parameters during this part of our study. During our analysis, we found that on increasing the thickness of SMA lamina, the maximum deflection in the vertical direction decreased. The explanation to this was found, as the thickness of ply increases, so does the equivalent stiffness of the lamina which primarily reduces the coupling stiffness and bending stiffness hence impeding deflection. The results capturing this response are shown in Fig. 6b.

Before we move to the analysis of composites with two layers of the SMA fiber-reinforcement, a bimorph, we examine the deflection obtained when the SMA fiber orientation angle is altered. We check the deflection profile for 30° , 45° , 60° , and 90° fiber orientation angles.

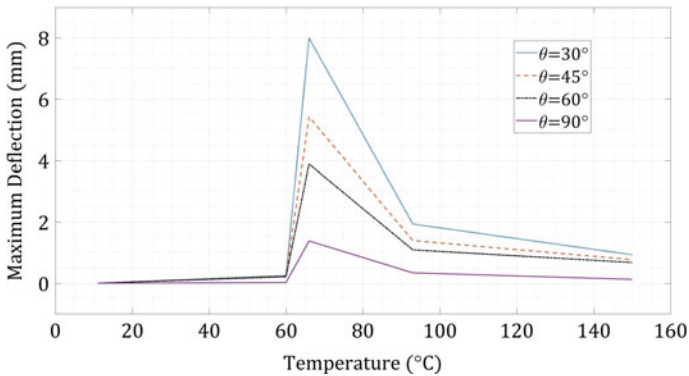
It was observed (refer Fig. 7a) that there was a huge drop in the deflection value in the vertical z-direction, caused due to the twisting of the plate about x-direction as we increased the orientation angle. For future work, wherein the requirement is of a twisting behavior, analysis with varying orientation angles is recommended. There is a 95% drop in maximum deflection along z-direction as soon as the fiber orientation angle is changed from 0° to 30° . The deflection keeps decreasing as the orientation angle reaches 90° , where the deflection is only 0.33 mm, resulting due to the transverse constraint. However, the maximum deflection along y-direction suddenly increases by 92% as the SMA fiber orientation angle changes from 0° to 30° but subsequently decreases with increase in fiber orientation angle as shown in Fig. 7b. While studying the effect of the orientation angles of the SMA fibers, we concluded that the twisting due to angled plies can be utilized for morphing applications where bidirectional bending is involved.

In the next phase of our work, we study the deflection profile of the active composite by adding another ply of SMA-Silicone at 90° SMA fiber orientation. A considerable decrease in deflection is caused. When both the layers are actuated, they tend to shrink orthogonally to each other, thus canceling out bending in either direction. This bimorph, as demonstrated in previous experiments by the authors [26], is modeled by introducing another E-glass fiber-Silicone rubber matrix ply at an offset, the ply layup then becomes $[0_{SMA}/0_f/0_{SMA}/0_f]$. In Fig. 8a and b, we see the effect of change in SMA fiber volume fraction on the bimorph, and effect of change in the thickness of SMA fiber ply, respectively.

The results we see in the current case are analogous to the previous case; the deflection increases as we increase the SMA fiber volume fraction and decreases as we increase the thickness of the SMA fiber ply. The speculated reasons are discussed previously. To observe the bidirectional bending, we consider the best case we have reckoned—SMA fiber volume fraction = 0.9 and ply thickness = 1 mm. An increase



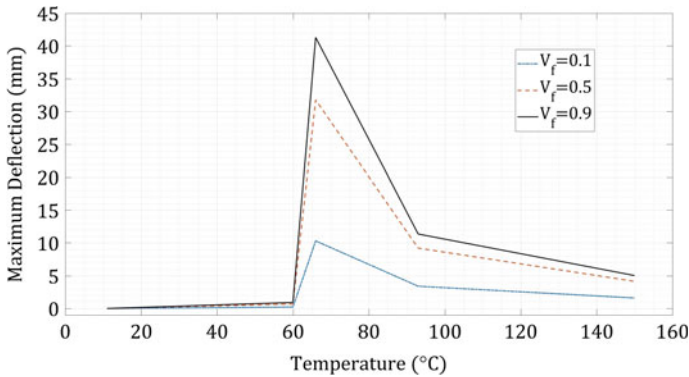
(a) Temperature vs maximum deflection along z-direction (bending about y-axis), SMA fiber ply thickness (t_{SMA})=1mm, SMA Fiber Volume Fraction (V_f)= 0.9



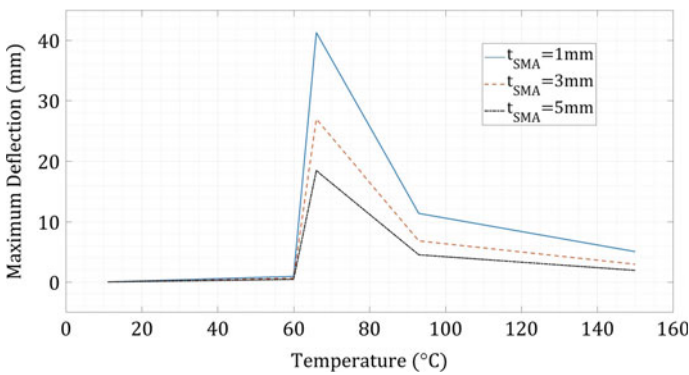
(b) Temperature vs maximum deflection along y-direction (bending about x-axis), SMA fiber ply thickness (t_{SMA})=1mm, SMA fiber volume fraction (V_f)=0.9

Fig. 7 Case 1.1: One layer of SMA fiber-reinforcement: temperature versus maximum deflection with varying SMA fiber orientation angle

in the deflection along y-axis was evident. This observation opens up the opportunity for advanced research in optimizing the location, SMA fiber volume fraction, and the thickness of the plies to get the required bimorph behavior. The maximum deflection along the y-axis, in this case, was found to be 1.444 mm, at 66 °C, 5 mm SMA fiber ply thickness, and 0.5 SMA fiber volume fraction. The deflection value seems to be small but is 80% higher from the analogous single layer SMA fiber ply case. Thus calculating the optimum location of the SMA fiber-reinforced plies in the layup is essential.



(a) Temperature vs maximum deflection, SMA fiber ply thickness (t_{SMA})=1mm



(b) Temperature vs maximum deflection, SMA fiber volume fraction (V_f)=0.9

Fig. 8 Case 1.2: Two layers of SMA fiber-reinforcement: temperature versus maximum deflection

Upon changing the boundary condition of the single SMA layer model from fixed-free to fixed-fixed, an exponential drop in deflection is observed caused due to further constraining thus restricting the shrinking of the SMA fiber (shape memory effect) upon thermal actuation. This causes the SMA fiber to undergo both stress-induced and temperature-induced phase transformation, unlike the previous case where only the temperature-induced phase transformation occurred. The maximum deflection along z-direction observed in a single layer of SMA fiber ply composite was very low, of the order of 1.39 mm, which further reduced in case of the bimorph to the order of 0.01 mm, at 66 °C when the reverse-phase transformation activates. The maximum deflection along y- and z-direction at varying temperatures for single-layer SMA fiber ply is shown in Fig. 9.

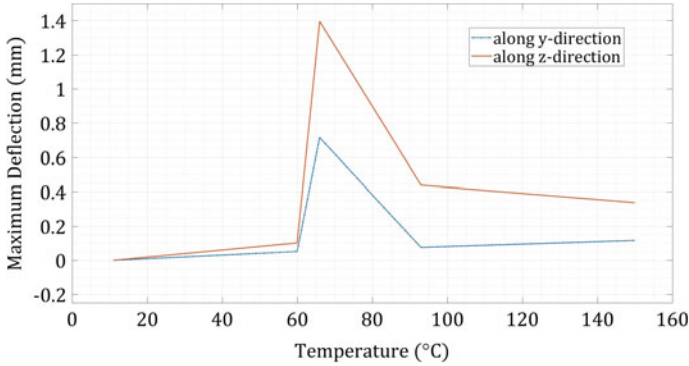


Fig. 9 Case 2: One layer of SMA fiber-reinforcement: temperature versus maximum deflection in the vertical direction when SMA fiber ply thickness (t_{SMA}) = 1 mm, SMA fiber volume fraction (V_f) = 0.9

As the thermal field is applied and the temperature is elevated, in-plane compressive stresses in the fixed-fixed plate are introduced, and due to shape memory effect, recovery stress is generated, causing the plate to deflect slightly which can be seen in Fig. 9. In both cases, the plate retains some residual strain, which can be almost completely be removed as the structure is cooled down.

4 Conclusion

Static thermoelastic response analysis of an SMA-based Active Bimorph Composite is explored in this paper. The ECTE model is employed to calculate the coefficient of thermal expansion for SMA from experimental results and is then employed in the simulation. The SMA fibers, having a negative coefficient of thermal expansion during reverse-phase transformation, act as an actuator for the plate when embedded at an offset. The structure was subjected to a uniformly elevating temperature field and was allowed to bend freely under the effect of its ECTE variation for two boundary conditions—fixed-free and fixed-fixed. In addition to this, the SMA fiber orientation angle, the thickness of SMA layer ply, and the SMA fiber volume fraction were varied, and the inferences made are presented in the paper.

We found that upon thermal actuation, the deflection of the plate reduces considerably in the case of two layers of SMA fiber-reinforced composite (SMA-ABHC); however, a bimorph behavior is successfully extracted. In applications, which require bidirectional bending, or shape morphing, an actively controlled bimorph is of vital importance. In our work, we aim to utilize this functionality for the rigidization purpose of space inflatable structures.

For future work on this subject, a detailed parametric study incorporating the effect of varying fiber orientation angle of both the layers of SMA fiber-reinforcement,

variation of SMA fiber ply thickness, and volume fraction on the deflection profile and the natural frequency of the SMA-AHBC can give a better insight and lay the ground for active shape control applications. For those who want to understand the behavior of the SMA-AHBC using only the resistive heating method can have electrical resistive heating modeled as a distributed heat source along the SMA fibers. This idea can also be utilized to have structures with varying stiffnesses and damping capacity over a broad temperature range.

Acknowledgements The authors would like to thank Mr. Praveen Kumar D. for his contribution in experiments of SMA characterization. This work was supported by the Indo-US Science and Technology Forum sponsored project: IUSSTF/ME/2017400A.

Appendix A

Reduced Stiffness Matrix and Rule-of-Mixtures

$$\begin{aligned} Q_{11} &= \frac{E_1}{1 - \nu_{12}\nu_{21}} & Q_{12} &= \frac{\nu_{12}E_2}{1 - \nu_{12}\nu_{21}} \\ Q_{22} &= \frac{E_2}{1 - \nu_{12}\nu_{21}} & Q_{66} &= G_{12} \end{aligned} \quad (7)$$

$$\begin{aligned} E_1 &= E_a \nu_a + E_{1m} \nu_m & E_2 &= \frac{E_a E_{2m}}{E_a \nu_m + E_{2m} \nu_a} \\ \nu_{12} &= \nu_a \nu_a + \nu_{12m} \nu_m & G_{12} &= \frac{G_a G_{12m}}{G_a \nu_m + G_{12m} \nu_a} \\ \int_{T_o}^T \alpha_1(\tau) d\tau &= \frac{E_a \nu_a \int_{T_o}^T \alpha_{1a}(\tau) d\tau + E_{1m} \nu_m \int_{T_o}^T \alpha_{1m}(\tau) d\tau}{E_a \nu_a + E_{1m} \nu_m} \\ \text{sgn}(\alpha_{1a}) &= \begin{cases} +1 & T < A_s \\ -1 & T \geq A_s \end{cases} \\ \int_{T_o}^T \alpha_2(\tau) d\tau &= \int_{T_o}^T [\alpha_{2a}(\tau) \nu_a + \alpha_{2m}(\tau) \nu_m] d\tau \end{aligned} \quad (8)$$

where the subscripts a and m indicate SMA and composite matrix constituents, respectively, E , ν , G , α are the Young's modulus, Poisson's ratio, shear modulus, and effective coefficient of thermal expansion respectively.

References

1. Allred R, Hoyt A, Scarborough S, Cadogan D, McElroy P UV rigidizable carbon-reinforced isogrid inflatable booms. In: 43rd AIAA/ASME/ASCE/AHS/ASC structures, structural dynamics, and materials conference . <https://doi.org/10.2514/6.2002-1202>
2. Auricchio F, Lubliner J (1997) A uniaxial model for shape-memory alloys. *Int J Solids Struct* 34(27):3601–3618. [https://doi.org/10.1016/S0020-7683\(96\)00232-6](https://doi.org/10.1016/S0020-7683(96)00232-6)
3. Auricchio F, Taylor R, Lubliner J (1997) Shape-memory alloys: macromodelling and numerical simulations of the superelastic behavior. *Comput Methods Appl Mech Eng* 146(3):281–312. [https://doi.org/10.1016/S0045-7825\(96\)01232-7](https://doi.org/10.1016/S0045-7825(96)01232-7)
4. Boyd J, Lagoudas D (1996) A thermodynamical constitutive model for shape memory materials. part I: the monolithic shape memory alloy. *Int J Plast* 12(6):805–842. [https://doi.org/10.1016/S0749-6419\(96\)00030-7](https://doi.org/10.1016/S0749-6419(96)00030-7)
5. Brinson L (1993) One-dimensional constitutive behavior of shape memory alloys: thermomechanical derivation with non-constant material functions and redefined martensite internal variable. *J Intell Mater Syst Struct* 4(2):229–242. <https://doi.org/10.1177/1045389X9300400213>
6. Buehler WJ, Wang FE (1965) Nickel-based alloys, U.S. Patent 3174851
7. Cadogan D, Scarborough S Rigidizable materials for use in gossamer space inflatable structures
8. Chandra R (2001) Active shape control of composite blades using shape memory actuation. *Smart Mater Struct* 10(5):1018–1024. <https://doi.org/10.1088/0964-1726/10/5/318> Oct
9. Daniel IM (2005) *Engineering mechanics of composite materials*, 2nd edn. Oxford University Press
10. Epps JJ, Chopra I (2001) In-flight tracking of helicopter rotor blades using shape memory alloy actuators. *Smart Mater Struct* 10(1):104–111. <https://doi.org/10.1088/0964-1726/10/1/310> Feb
11. Escher K, Hornbogen E (1991) Robot grippers—an application of two-way shape memory. In: Eucken s (ed) *Progress in shape memory*, pp 301–316
12. Ghomshei MM, Khajepour A, Tabandeh N, Behdina K (2001) Finite element modeling of shape memory alloy composite actuators: theory and experiment. *J Intell Mater Syst Struct* 12(11):761–773. <https://doi.org/10.1177/104538901400438055>
13. Hartl DJ, Lagoudas DC, Calkins FT, Mabe JH (2009) Use of a Ni60Ti shape memory alloy for active jet engine chevron application: I. Thermomechanical characterization. *Smart Mater Struct* 19(1):015020. <https://doi.org/10.1088/0964-1726/19/1/015020> Dec
14. Jenkins CHM (2001) Gossamer spacecraft: membrane and inflatable structures technology for space applications. In: *Progress in astronautics and aeronautics*, American institute of astronautics and aeronautics, Inc. 191. <https://doi.org/10.2514/4.866616>
15. Jia J, Rogers CA (1989) Formulation of a mechanical model for composites with embedded SMA actuators. In: *Proceedings of the 8th biennial ASME conference on failure prevention and reliability*. <https://doi.org/10.1115/1.2917059>
16. Kumar P, Bhattacharya B (2013) Active shape control of parabolic antenna using shape memory alloy wires
17. Lagoudas DC, Bo Z, Qidwai MA, Entchev PB (2003) User material subroutine for thermomechanical constitutive model of shape memory alloys. *SMA User Man*
18. Liang C, Rogers C (1990) One-dimensional thermomechanical constitutive relations for shape memory materials. *J Intell Mater Syst Struct* 1(2):207–234. <https://doi.org/10.1177/1045389X9000100205>
19. Meo M, Antonucci E, Duclaux P, Giordano M (2005) Finite element simulation of low velocity impact on shape memory alloy composite plates. *Compos Struct* 71(3):337–342. <https://doi.org/10.1016/j.compstruct.2005.09.029>. Fifth international conference on composite science and technology
20. Panda SK, Singh BN (2010) Thermal post-buckling analysis of a laminated composite spherical shell panel embedded with shape memory alloy fibres using non-linear finite element method. *Proc Inst Mech Eng, Part C: J Mech Eng Sci* 224(4):757–769. <https://doi.org/10.1243/09544062JMES1809>

21. Pinto F, Ciampa F, Meo M, Polimeno U (2012) Multifunctional SMARt composite material for in-situ NDT/SHM and de-icing. *Smart Mater Struct* 21(10):105010. <https://doi.org/10.1088/0964-1726/21/10/105010>
22. Rogers CA, Robertshaw HH (1988) Shape memory alloy reinforced composites. *Eng Sci Prepr, Soc Eng Sci Inc.* 25
23. Salichs J, Hou Z, Noori M (2001) Vibration suppression of structures using passive shape memory alloy energy dissipation devices. *J Intell Mater Syst Struct* 12(10):671–680. <https://doi.org/10.1106/RGRQ-VJKM-QWCF-QQDE>
24. Sittner P, Sedlák P, Seiner H, Sedmák P, Pilch J, Delville R, Heller L, Kadeřávek L (2018) On the coupling between martensitic transformation and plasticity in NiTi: experiments and continuum based modelling. *Prog Mater Sci* 98:249–298. <https://doi.org/10.1016/j.pmatsci.2018.07.003>
25. Sofla A, Meguid S, Tan K, Yeo W (2010) Shape morphing of aircraft wing: status and challenges. *Mater Des* 31(3). <https://doi.org/10.1016/j.matdes.2009.09.011>
26. Srivastava R, Sharma AK, Hait AK, Bhattacharya B (2018) Design and development of active bimorph structure for deployable space application 10595. <https://doi.org/10.1117/12.2296547>
27. Stiles L, Schaub H, Maute K, Moorer D Electrostatic inflation of membrane space structures. In: AIAA/AAS astrodynamics specialist conference. <https://doi.org/10.2514/6.2010-8134>
28. Tanaka K (1986) A thermomechanical sketch of shape memory effect: one-dimensional tensile behavior. *Int J Struct Mech Mater Sci, Res Mech* 18
29. Turner TL (2000) A new thermoelastic model for analysis of shape memory alloy hybrid composites. *J Intell Mater Syst Struct* 11(5):382–394. <https://doi.org/10.1106/DTFJ-UFL3-XV0U-WJNA>
30. Turner T, Zhong Z, Mei C (1994) Finite element analysis of the random response suppression of composite panels at elevated temperatures using shape memory alloy fibers. In: Proceedings of the 35th structures, structural dynamics and materials conference. <https://doi.org/10.2514/6.1994-1324>